Physics of the Earth and Planetary Interiors 292 (2019) 12–20

Contents lists available at ScienceDirect

Physics of the Earth and Planetary Interiors

journal homepage: www.elsevier.com/locate/pepi

Imaging Yellowstone magmatic system by the joint Gramian inversion of gravity and magnetotelluric data

Michael Jorgensen*, Michael S. Zhdanov

Consortium for Electromagnetic Modeling and Inversion, University of Utah, Salt Lake City, UT 84112, United States
TechnoImaging, Salt Lake City, UT 84107, United States

ARTICLE INFO

Keywords:
Magnetotellurics
Gravity
Joint inversion
Yellowstone

ABSTRACT

Gravity and long-period magnetotelluric data are combined in a joint Gramian inversion to obtain structurally-similar 3D density and electrical resistivity models of the Yellowstone magmatic feeding system. Structural constraints are enforced through a correlation of the model gradients. Gravity data are sensitive to upper-crustal structure, whereas long-period magnetotelluric data are more sensitive to deeper structure. By combining these complementary data, the jointly inverted models provide a consistent image of the partially molten structure underlying the Yellowstone Caldera from the surface to the Moho. Discrete zones of inferred partial melt in the upper and lower crust are fed by a southwest trending plume, and satisfy expectations from modern mantle plume models.

1. Introduction

The deep magma-feeding structures underlying volcanoes are often poorly resolved. To better resolve these structures, integration of all available data needs to be done; however, this has not been done at Yellowstone. We partially address this problem by jointly inverting existing gravity and magnetotelluric (MT) data using a joint inversion based on Gramian constraints (Zhdanov et al., 2012). The various geophysical data are complementary for subsurface characterization, making it natural to consider a formal mathematical framework for their joint inversion to a shared model of Yellowstone. In particular, the gravity method is generally more sensitive to density and upper-crustal structure, whereas long-period MT sites are more sensitive to resistivity and deeper structure. By exploiting the strengths of both methods in a joint inversion, we gain the benefit of limiting null space in the models. By structurally constraining each physical property distribution with the other, we obtain uniform spatial boundaries of anomalous zones, to be demonstrated.

There are two main approaches to the joint inversion of geophysical data: a direct petrophysical correlation, or a structural correlation. In the petrophysical approach, direct correlation or anti-correlation is assumed to exist between the modeled geophysical properties (DeStefano et al., 2011; Moorkamp et al., 2013). This approach is dependent on the validity of the petrophysical operator, which may be constituted using some empirical relation (e.g., Archie's law) or stochastically from well-logs (Colombo and Rovetta, 2018). Haber and Oldenburg (1997) developed a framework for the structural approach, which is not dependent on a direct correlation between the modeled parameters. In this approach, structural similarity between the models is based on the correlation of a model property such as the gradient, Laplacian, etc. An applied example of the structural approach is the cross-gradients method of Gallardo and Meju (2003). Zhdanov et al. (2012) introduced a unified approach to joint inversion using Gramian constraints. In this generalized approach, it can be shown that methods based on direct correlations and/or structural constraints are special case reductions. Zhdanov et al. (2016) applied this approach to airborne electromagnetic and potential field data. We present an application of the Gramian approach to the joint inversion of gravity and MT data.

The inversion workflow consists of performing standalone 3D inversions of the gravity and MT data to select appropriate inversion parameters. This information is passed as input to the joint 3D inversion using Gramian constraints. The results of standalone and joint inversions are compared for a synthetic model of Yellowstone to demonstrate the efficacy of the developed method and algorithm. We then apply our method to the joint inversion of gravity and MT data acquired around Yellowstone National Park.

Basaltic and rhyolitic volcanism has migrated northeastward along the Yellowstone Snake River Plain (YSRP) axis during the late Cenozoic, possibly due to interactions with a deep mantle plume (Hadley et al.,

* Corresponding author at: Consortium for Electromagnetic Modeling and Inversion, University of Utah, Salt Lake City, UT 84112, United States.
E-mail address: mike.jorgensen@utah.edu (M. Jorgensen).

https://doi.org/10.1016/j.pepi.2019.05.003
Received 22 March 2019; Received in revised form 30 April 2019; Accepted 1 May 2019
Available online 08 May 2019

1976; Smith and Braile, 1994; Smith et al., 2009). The Yellowstone region is composed of an outer zone with rhyolitic ash-flow tuffs, small rhyolitic lava flows, and basaltic sheets; and an inner zone with very large rhyolitic lava flows (Boyd, 1961). The large Basin and Range type faults surrounding Yellowstone are terminated on or near the caldera rims; therefore, these structures apparently existed before the arrival of the Yellowstone hotspot to its current location (Glen and Ponce, 2002; Zoback and Thompson, 1978). They were destroyed on the surface by the large caldera-forming eruptions; however, they are still present at depth. Therefore, one of the important goals of studying the Yellowstone volcanic system is understanding how the caldera interacts with the magma-feeding system at depth.

We focus on constructing the deep magma-feeding structure of the Yellowstone volcanic system. Until recently, this problem was primarily studied using seismic methods (e.g. Farrell et al., 2014; Smith et al., 2009). These models commonly resolve a discontinuous low-velocity zone extending into the upper mantle. The shallowest ($<$ 20 km depth) component of this zone has broadly been interpreted as rhyolitic partial melt, which fails to explain the high CO_2 flux measured in the caldera (Lowenstern and Hurwitz, 2008). More recently, Huang et al. (2015) resolved a distinct lower-crustal low velocity zone interpreted as basaltic partial melt–providing a magmatic link between the mantle plume and the upper-crustal partial melt. In the last decade, various density models have been developed (e.g. DeNosaquo et al., 2009) which commonly resolve an upper-crustal low density zone consistent with an interpretation of rhyolitic partial melt. Various resistivity models have also been developed (Cuma et al., 2017; Kelbert et al., 2012; Meqbel et al., 2014; Zhdanov et al., 2011), which commonly resolve a deep conductive mantle plume, but widely vary with respect to crustal structure. We develop and present images of the Yellowstone magmatic system which share common structure from the surface to the Moho.

2. Forward modeling

Gravity data, $\mathbf{g}_z$, are calculated with the following integral formula:

$$\mathbf{g}_z(\mathbf{r}') = \gamma \iiint_D \rho(\mathbf{r}) \frac{\mathbf{r}-\mathbf{r}'}{|\mathbf{r}-\mathbf{r}'|^3} dv, \tag{1}$$

where γ is the universal gravitational constant and $\rho(\mathbf{r})$ is the anomalous density distribution.

We also utilize all components of the MT impedance tensor. The total EM fields used to determine impedance values are calculated with the following integral equations (Zhdanov and Keller, 1992):

$$\mathbf{E}(\mathbf{r}') = \mathbf{E}^b(\mathbf{r}') + \iiint_D \widehat{\mathbf{G}}_E(\mathbf{r}' \mid \mathbf{r}) \Delta\sigma(\mathbf{r})(\mathbf{E}^b(\mathbf{r}) + \mathbf{E}^a(\mathbf{r}))dv, \tag{2}$$

$$\mathbf{H}(\mathbf{r}') = \mathbf{H}^b(\mathbf{r}') + \iiint_D \widehat{\mathbf{G}}_H(\mathbf{r}' \mid \mathbf{r}) \Delta\sigma(\mathbf{r})(\mathbf{E}^b(\mathbf{r}) + \mathbf{E}^a(\mathbf{r}))dv, \tag{3}$$

where $\widehat{\mathbf{G}}_E(\mathbf{r}' \mid \mathbf{r})$ and $\widehat{\mathbf{G}}_H(\mathbf{r}' \mid \mathbf{r})$ are the electric and magnetic Green's tensors and $\Delta\sigma(\mathbf{r})$ is the anomalous conductivity distribution. We use the contraction integral equation method of Hursan and Zhdanov (2002) to solve Eqs. (2) and (3). More details about the computer implementation of the integral equation method for MT field modeling can be found in Zhdanov (2018).

3. Joint inversion with Gramian constraints

The gravity and MT inverse problems can be written in the form of the following operator equations:

$$\mathbf{m}^{(i)} = \mathbf{A}^{(i)-1}\mathbf{d}^{(i)},\ i = 1, 2, \tag{4}$$

where $\mathbf{d}^{(i)}$, $(i = 1,2)$ are the observed gravity and MT data, and $\mathbf{m}^{(i)}$, $(i = 1,2)$ are the unknown density and geoelectrical resistivity distributions, respectively. Following the principles of Tikhonov regularization (Tikhonov and Arsenin, 1977) and Gramian stabilization (Zhdanov, 2015), we solve Eq. (4) by minimizing the following joint parametric functional:

$$P^\alpha(\mathbf{m}^{(1)}, \mathbf{m}^{(2)}) = \sum_{i=1}^{2} \varphi^{(i)}(\mathbf{m}^{(i)}) + \sum_{i=1}^{2} \alpha^{(i)} s_{MN}(\mathbf{m}^{(i)}) + \beta s_G(\nabla\mathbf{m}^{(1)}, \nabla\mathbf{m}^{(2)}) \tag{5}$$

where the terms $\varphi^{(i)}$ are the data misfit functionals:

$$\varphi^{(i)}(\mathbf{m}^{(i)}) = \|\mathbf{W}_d^{(i)}(\mathbf{A}^{(i)}(\mathbf{m}^{(i)}) - \mathbf{d}^{(i)})\|^2,\ i = 1, 2, \tag{6}$$

$\mathbf{W}_d{}^{(i)}$ are the data weighting operators, and $\mathbf{A}^{(i)}$ are the forward modeling operators. The terms $s_{MN}(\mathbf{m}^{(i)})$ are the minimum norm stabilizing functionals:

$$s_{MN}(\mathbf{m}^{(i)}) = \|\mathbf{W}_m^{(i)}(\mathbf{m}^{(i)} - \mathbf{m}_{apr}^{(i)})\|^2,\ i = 1, 2, \tag{7}$$

where $\mathbf{W}_m{}^{(i)}$ are the model weighting operators, and $\mathbf{m}_{apr}{}^{(i)}$ are the a priori models. The Gramian constraint term for structural correlation of the models is defined as follows:

$$s_G(\nabla\mathbf{m}^{(1)}, \nabla\mathbf{m}^{(2)}) = \begin{vmatrix} (\nabla\mathbf{m}^{(1)}, \nabla\mathbf{m}^{(1)}) & (\nabla\mathbf{m}^{(1)}, \nabla\mathbf{m}^{(2)}) \\ (\nabla\mathbf{m}^{(2)}, \nabla\mathbf{m}^{(1)}) & (\nabla\mathbf{m}^{(2)}, \nabla\mathbf{m}^{(2)}) \end{vmatrix}. \tag{8}$$

where $\nabla\mathbf{m}^{(i)}$ are the model gradients. The determinant is basically a measure of two gradients being parallel, similar to the cross-gradient method. As we minimize this term, the model gradients become parallel, enforcing structural similarity. Finally, the terms $\alpha^{(i)}$ and β are adaptive regularization parameters which monotonically decrease the stabilizers. The first iteration is run with these parameters set to zero, or no regularization. After the first iteration, the initial values are determined as follows:

$$\alpha_0^{(i)} = \frac{\varphi^{(i)}(\mathbf{m}^{(i)})}{s_{MN}(\mathbf{m}^{(i)})}, \tag{9}$$

$$\beta_0 = \frac{\varphi^{(i)}(\mathbf{m}^{(i)})}{s_G(\nabla\mathbf{m}^{(1)}, \nabla\mathbf{m}^{(2)})}, \tag{10}$$

and regularization on subsequent iterations is determined by the following progression of numbers:

$$\alpha_n^{(i)} = \alpha_0^{(i)} q^n,\ q < 1, \tag{11}$$

$$\beta_n = \beta_0 q^n,\ q < 1, \tag{12}$$

where n is indexed up on iterations where the data misfit fails to decrease by 1% relative to the misfit on the previous iteration, and $q = 0.95$.

Model parameters are normalized by a function of the sensitivity:

$$\mathbf{W}_m^{(i)} = diag(\sqrt[4]{\mathbf{F}_m^{(i)T}\mathbf{F}_m^{(i)}}), \tag{13}$$

where $\mathbf{F}_m{}^{(i)}$ is the Fréchet derivative of $\mathbf{A}^{(i)}(\mathbf{m}^{(i)})$. This normalization ensures the uniform sensitivity of the data to the normalized model parameters. Matrices $\mathbf{W}_m{}^{(i)}$ are stored as sparse $m \times m$ diagonal matrices.

The model parameters are further scaled in the joint inversion such that they are approximately bounded between $[-1,1]$ with the following transform:

$$\widetilde{\mathbf{m}}^{(i)} = \frac{\mathbf{W}_m^{(i)}(\mathbf{m}^{(i)} - \mathbf{m}_b^{(i)})}{max\ |\mathbf{W}_m^{(i)}(\mathbf{m}^{(i),sep} - \mathbf{m}_b^{(i)})|}, \tag{14}$$

where $\mathbf{m}^{(i),\ sep}$ is obtained from standalone inversion, and $\mathbf{m}_b{}^{(i)}$ is the model background.

The data weights, $\mathbf{W}_d{}^{(i)}$, are computed component-wise by the mean of the gravity data and the variance of the MT data, stored as $d \times d$ matrices, and yield the transforms:

$$\widetilde{\mathbf{d}}^{(i)} = \mathbf{W}_d^{(i)}\mathbf{d}^{(i)}, \tag{15}$$

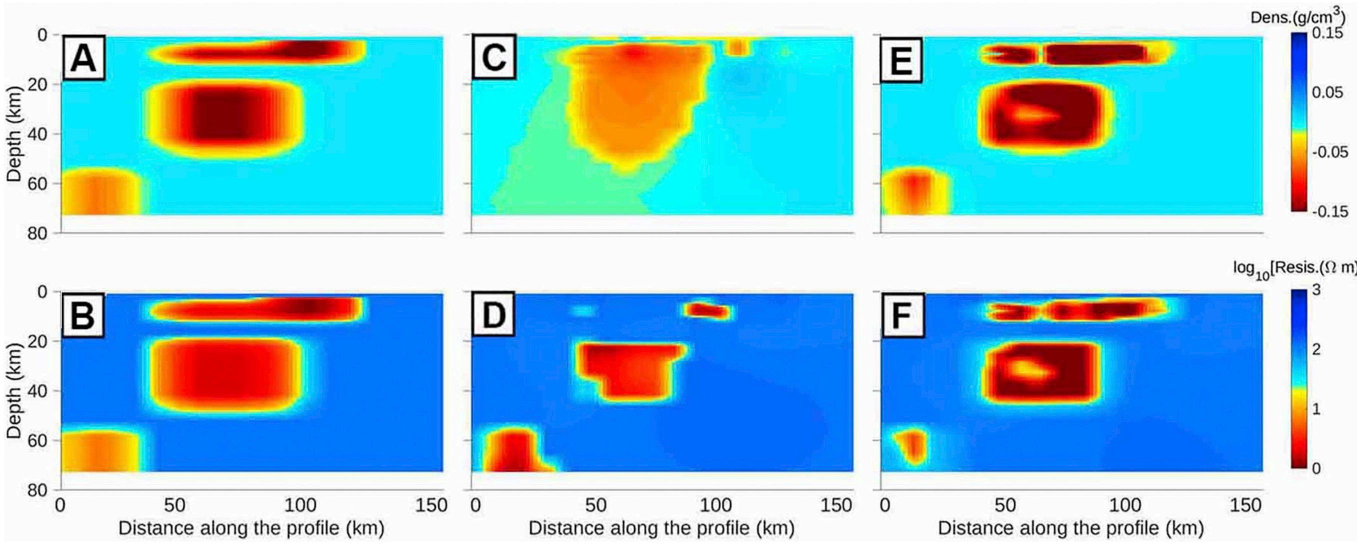

Fig. 1. Vertical sections of the synthetic model: panels A and B show true anomalous density and total resistivity models, respectively; panels C and D present the standalone inverted density and resistivity models; panels E and F show the jointly inverted density and resistivity models, respectively.

$$\widetilde{\mathbf{A}}^{(i)}(\widetilde{\mathbf{m}}^{(i)}) = \mathbf{W}_d^{(i)}\mathbf{A}^{(i)}(\widetilde{\mathbf{m}}^{(i)}). \tag{16}$$

The error floors of 5% are imposed on the impedances. The data are further scaled in the joint inversion such that the data misfits on the first iteration are unity:

$$\varphi_1^{(i)}(\widetilde{\mathbf{m}}^{(i)}) = \frac{\|\widetilde{\mathbf{A}}^{(i)}\widetilde{\mathbf{m}}^{(i)} - \widetilde{\mathbf{d}}^{(i)}\|^2}{\|\widetilde{\mathbf{A}}^{(i)}\widetilde{\mathbf{m}}_{ini}^{(i)} - \widetilde{\mathbf{d}}^{(i)}\|^2}, \tag{17}$$

where $\widetilde{\mathbf{m}}_{ini}^{(i)}$ is the initial model.

The parametric functional in Eq. (5) is minimized using the regularized conjugate gradient method outlined in (Zhdanov, 2015):

$$\begin{gathered}
\widetilde{\mathbf{r}}_k = \widetilde{\mathbf{A}}(\widetilde{\mathbf{m}}_k) - \widetilde{\mathbf{d}}, \\
\mathbf{l}_k^{\alpha} = \widetilde{\mathbf{F}}_m^T \mathbf{W}_d \widetilde{\mathbf{r}}_k + \alpha_k \mathbf{W}_m(\widetilde{\mathbf{m}} - \widetilde{\mathbf{m}}_{apr}) + \beta_k \mathbf{l}_{G\nabla}, \\
\beta_k^{\alpha} = \frac{\|\mathbf{l}_k^{\alpha}\|^2}{\|\mathbf{l}_{k-1}^{\alpha}\|^2}, \\
\widetilde{\mathbf{l}}_k^{\alpha} = \mathbf{l}_k^{\alpha} + \beta_k^{\alpha}\widetilde{\mathbf{l}}_{k-1}^{\alpha},\ \widetilde{\mathbf{l}}_0^{\alpha} = \mathbf{l}_0^{\alpha} \\
\widetilde{s}_k^{\alpha} = (\widetilde{\mathbf{l}}_k^{\alpha}, \mathbf{l}_k^{\alpha})/(\|\widetilde{\mathbf{F}}_{m_k}\widetilde{\mathbf{l}}_k^{\alpha}\|^2 + \alpha_k\ \|\widetilde{\mathbf{l}}_k^{\alpha}\|^2 + \beta_k\ \|\mathbf{G}_{m_k}\widetilde{\mathbf{l}}_k^{\alpha}\|^2), \\
\widetilde{\mathbf{m}}_{k+1} = \widetilde{\mathbf{m}}_k - \widetilde{s}_k^{\alpha}\widetilde{\mathbf{l}}_k^{\alpha},
\end{gathered} \tag{18}$$

where $\widetilde{\mathbf{d}}$ is a concatenated vector of the gravity and MT data

$$\widetilde{\mathbf{d}} = (\widetilde{\mathbf{d}}^{grav}, \widetilde{\mathbf{d}}^{MT})^T, \tag{19}$$

$\widetilde{\mathbf{m}}_k$ is a concatenated vector of the density and resistivity models computed at iteration k,

$$\widetilde{\mathbf{m}}_k = (\widetilde{\mathbf{m}}_k^{dens}, \widetilde{\mathbf{m}}_k^{resis})^T, \tag{20}$$

operator $\widetilde{\mathbf{A}}$ is a combined matrix of forward operators

$$\widetilde{\mathbf{A}} = \begin{bmatrix} \widetilde{\mathbf{A}}^{grav} & \\ & \widetilde{\mathbf{A}}^{MT} \end{bmatrix}, \tag{21}$$

and finally, the directions of the steepest ascent for the Gramian stabilizer in Eq. (18) are given by the following formula (Zhdanov, 2015):

$$l_{G\nabla}^{(i)} = \sum_{j=1}^{n} (-1)^{i+j} G_{ij}^{\nabla\widetilde{m}} \nabla^2 \widetilde{m}^{(j)} \tag{22}$$

If the data misfit converges far above the noise level, the Gramian constraint is relaxed, and the iterative process is terminated when the data misfit reaches the noise level or fails to decrease by 1% relative to the misfit on the previous iteration for three successive iterations.

4. Synthetic model study

We demonstrate the efficacy of the method of joint Gramian inversion of gravity and MT data with the synthetic model study shown in Fig. 1. We use the same inversion parameters, receiver locations, and data components from the case study in the next section; allowing us to verify depth resolution of the data. The geomorphology of the synthetic model is roughly based off the Huang et al. (2015) seismic velocity model. Three anomalous zones are modeled with different sizes, depths, and physical properties. The synthetic data are contaminated with 5% Gaussian noise added to the MT fields and 1% added to the gravity data.

The standalone inverse models highlight the depths where the respective methods lack resolution. The gravity data were largely insensitive to a priori density anomalies placed under the Moho (~45 km in this region). Conversely, the MT data were sensitive to conductors placed in the upper crust; however, they were not resolved by the standalone inversion without their inclusion a priori.

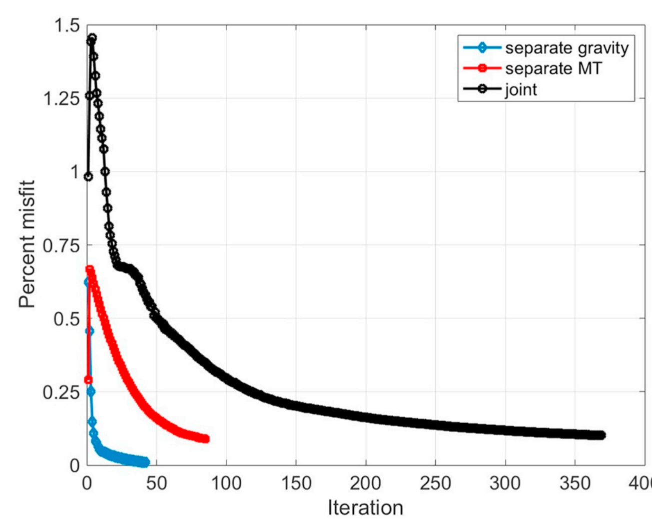

Fig. 2. Comparison of misfit convergence behavior of the standalone and joint inverse solutions to the synthetic model. The blue line corresponds to the standalone gravity misfit, the red line corresponds to the standalone MT misfit, and the black line corresponds to the joint misfit. (For interpretation of the references to color in this figure legend, the reader is referred to the web version of this article.)

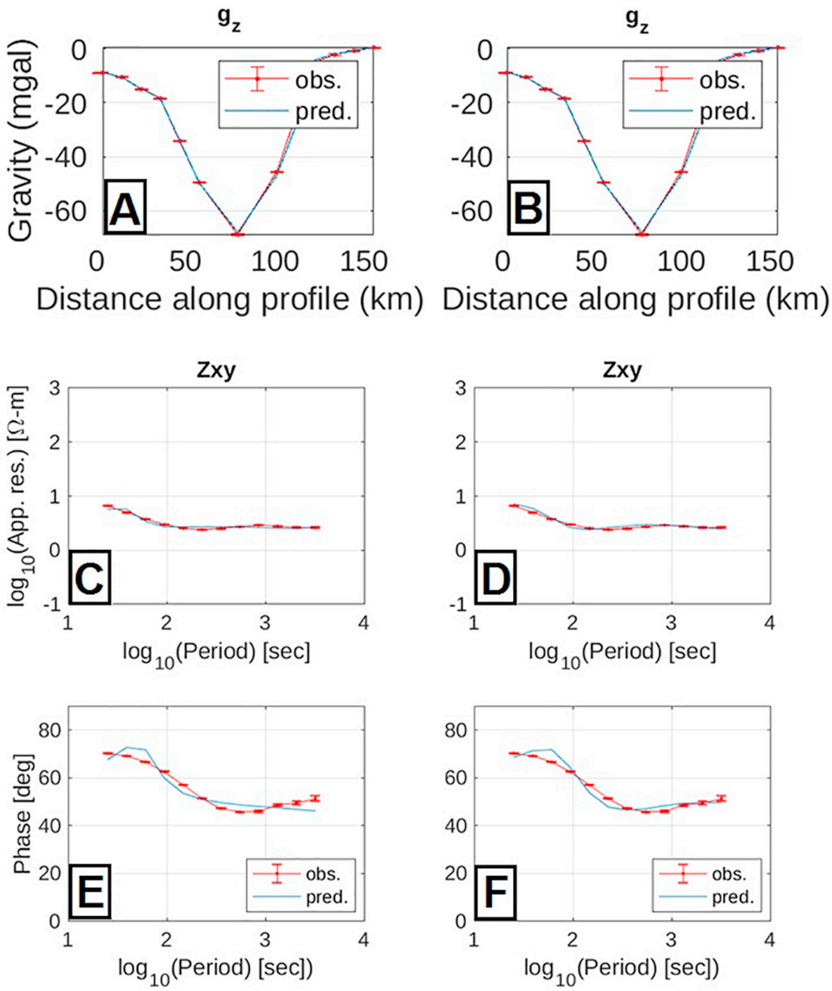

Fig. 3. Comparison of the observed and predicted data for standalone and joint synthetic inversions. The observed data are shown by the red lines and the blue lines depict the predicted data. Panels A and B show the comparison between the observed and predicted gravity data along profile AA′ shown in Fig. 4 obtained by standalone and joint inversions, respectively. Panels C and D show the comparison between the observed and predicted apparent resistivity for the XY principal impedance at the MT site shown by the green triangle in Fig. 4 obtained by standalone and joint inversions, respectively. Panels E and F show the comparison between the observed and predicted phase for the XY principal impedance at the same site obtained by standalone and joint inversions, respectively. (For interpretation of the references to color in this figure legend, the reader is referred to the web version of this article.)

We contrast the standalone inverse solutions with the jointly inverted solutions–both run from homogeneous starting models, where we find reasonable depth resolution throughout the domain with the added structural constraint. The jointly inverted models recover three distinct anomalies which mirror the true models with respect to size, shape, and location. Both standalone and joint inversions were terminated at a gravity RMS misfit of 0.1 and an MT RMS misfit of 1.5. A comparison of the misfit convergence behavior for the standalone and joint inversions is shown in Fig. 2. Observed and predicted data for the synthetic model are shown in Fig. 3.

5. Summary of the Yellowstone data

The Yellowstone area of the survey and the station map are shown in Fig. 4. The complete Bouguer anomaly data were downloaded from the North American gravity database (Hinze et al., 2005). These data were interpolated onto an equidistantly-spaced grid (10 km spacing), Fourier transformed, and bandpass filtered to eliminate effects from the overlying sedimentary basin and the deep mantle. The filter passed wavelengths of 40–500 km, which should correspond to a depth of investigation of roughly 6–83 km (Hinze et al., 2013). The complete Bouguer anomaly data used are shown in Fig. 5.

The MT data used in this study were collected as part of the EarthScope USArray project. MT station spacing is roughly 70 km with denser coverage provided by a YSRP transect. A significant static shift was found in the MT data, and was removed using the complex distortion tensor method of (Gribenko and Zhdanov, 2015; Gribenko and Zhdanov, 2017). A representative static shift correction is shown in Fig. 6. We fit the four components of the MT impedance tensor for all sites, using 16 periods from the interval of 20–3160 s.

6. Yellowstone inversion results and discussion

We applied the developed method to gravity and MT data gathered in the Yellowstone survey area. Inversion parameter testing yielded an optimal horizontal cell size of 7.75 km, with 36 logarithmically spaced vertical layers. The inversion domain is extended laterally to 400 × 400 km, and centered about Yellowstone. Both standalone and joint inversions were run with the homogeneous starting models (120 Ohm-m and -0.001 g/cm^3) to provide unbiased results. All inversions were run on a single 16-core Xeon compute node with 64 GB memory. The standalone inversions converged in 100–300 iterations, while the joint inversion ran for 900 iterations. Total runtime for the joint inversion was roughly 4 h. Both standalone and joint inversions were terminated at a gravity RMS misfit of 0.1 and an MT RMS misfit of 1.7, which was where the joint inversion converged.

The 3D inverse models are shown in a series of truncated vertical sections, and compare standalone and joint inverse solutions. The most striking features in Fig. 7 are two distinct zones of anomalous low density and resistivity directly underlying the caldera. We infer these to be zones of upper-crustal rhyolitic and lower-crustal basaltic partial melt (Huang et al., 2015; Lowenstern and Hurwitz, 2008), which appear to be fed by a deflected plume trending to the southwest. Traditional mantle plume models (e.g. Morgan, 1971) were constructed around a vertical plume; however, newer models (Steinberger et al., 2004) account for the deflection of plume material by convective

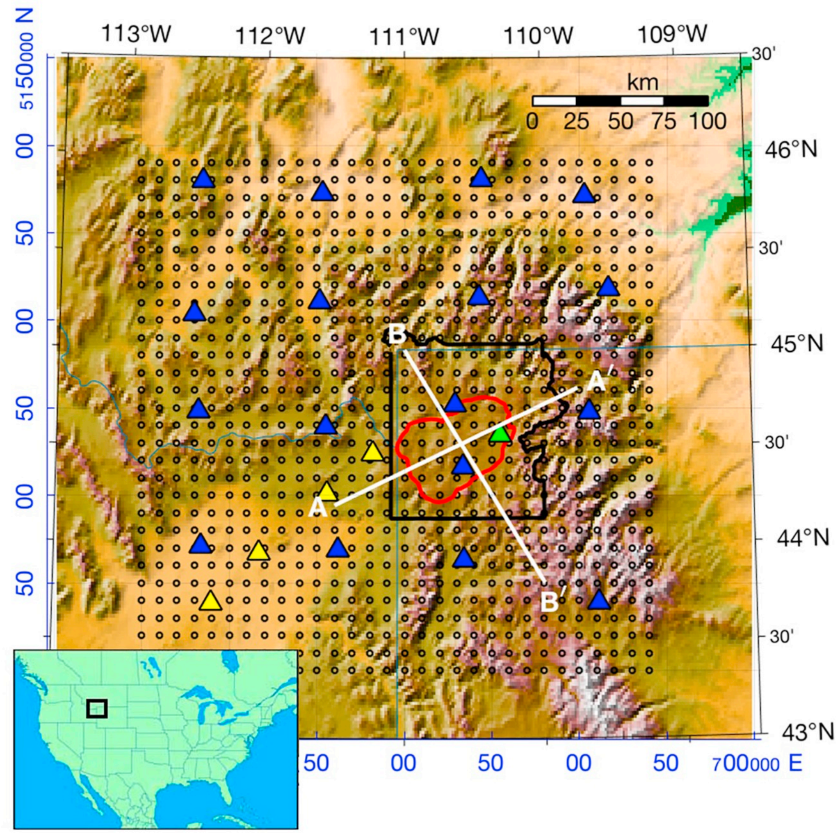

Fig. 4. Map of the gravity and MT stations used in this study and the locations of the vertical sections in the Yellowstone area. The Earthscope MT sites are marked by the blue triangles. The YSRP transect MT sites are shown by the yellow triangles. Observed and predicted data shown in Figs. 3 and 10 correspond the MT site marked by the green triangle. The interpolated gravity sites are marked by the black dots. The solid black line outlines the Yellowstone National Park boundary. The solid red line outlines the caldera. Solid blue lines indicate US state borders. The locations of the vertical sections in Figs. 7 and 11 are shown by the solid white lines with the labels. The insert map shows the location of the inversion domain (a black box). (For interpretation of the references to color in this figure legend, the reader is referred to the web version of this article.)

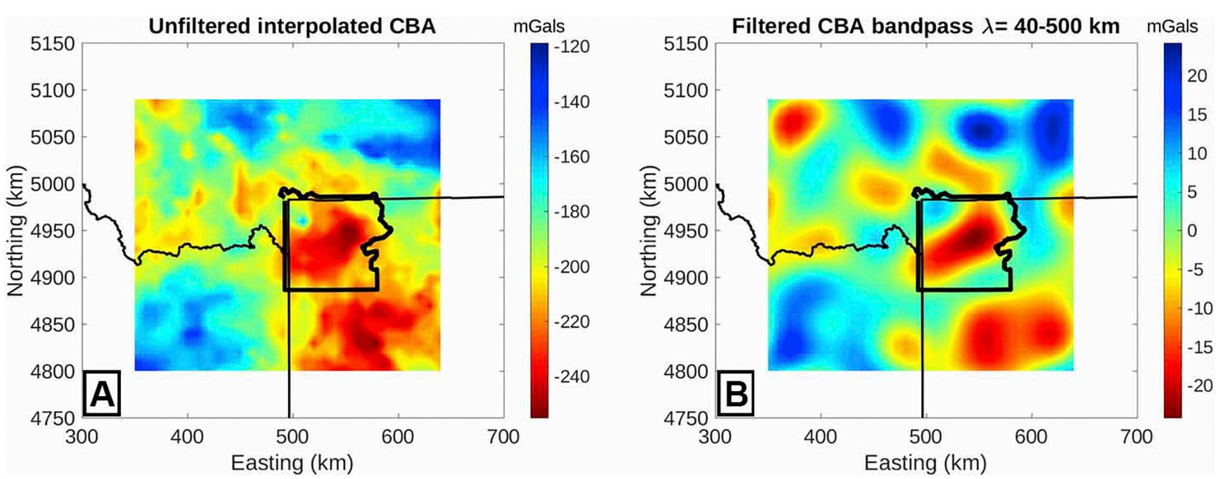

Fig. 5. Complete Bouguer anomaly data. Panels A and B present the maps of the unfiltered data and the bandpass filtered data used in the inversion, respectively.

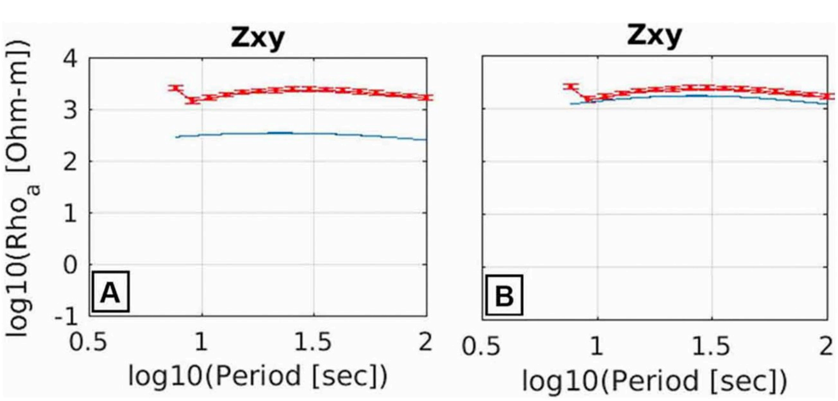

Fig. 6. Representative plots of the MT static shift correction. The observed data are shown by the red lines, while the blue lines represent the predicted data. One can see that static shift is present across all frequencies in the uncorrected impedances (A), but it is removed after correction using a complex distortion tensor (B). (For interpretation of the references to color in this figure legend, the reader is referred to the web version of this article.)

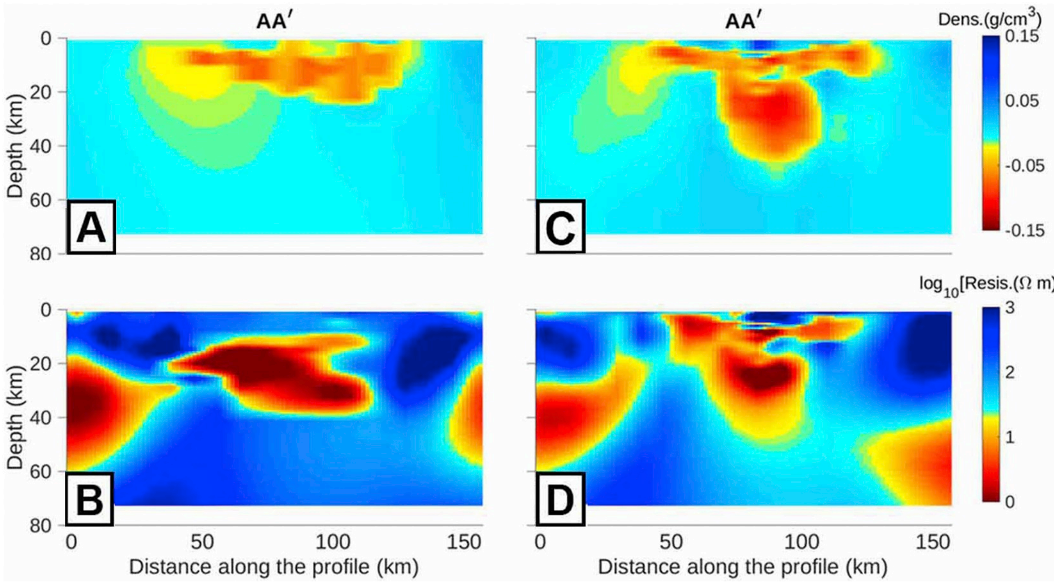

Fig. 7. Comparison of standalone and joint inverse solutions – vertical sections along line AA′. Panels A and B show the standalone inverted anomalous density and total resistivity models, respectively. Panels C and D present the jointly inverted density and resistivity models, respectively.

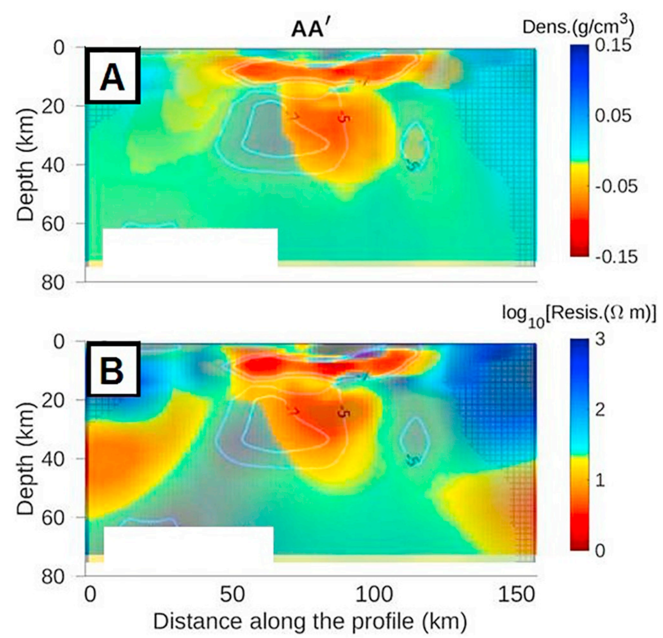

Fig. 8. Vertical sections of the joint inverse solutions along profile line AA′ with seismic velocity model from Huang et al. (2015) superimposed. Panel A shows the jointly inverted density model. Panel B shows the jointly inverted resistivity model.

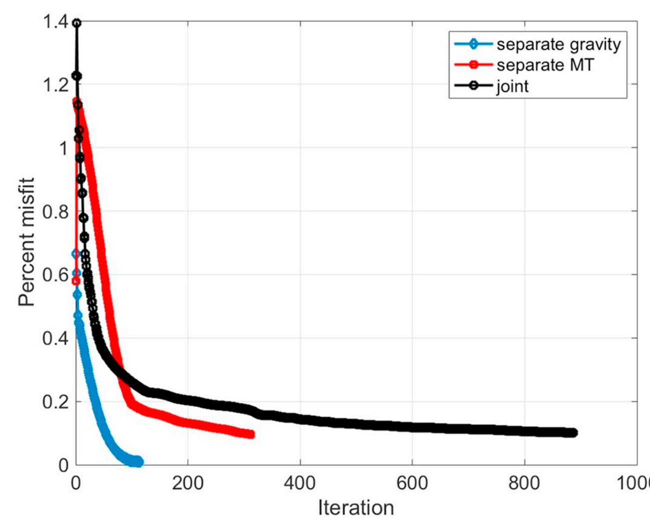

Fig. 9. Comparison of misfit convergence behavior of the standalone and joint inverse solutions to the Yellowstone model. The blue line corresponds to the standalone gravity misfit, the red line corresponds to the standalone MT misfit, and the black line corresponds to the joint misfit. (For interpretation of the references to color in this figure legend, the reader is referred to the web version of this article.)

mantle flow. The lateral extent of the rhyolitic zone is easily explained by advective heat transfer via hydrous fluid.

The boundaries of the anomalous zones are reasonably spatially consistent with anomalous low seismic velocity zones found by Huang et al. (2015) shown superimposed over our joint inverse solutions in Fig. 8. There is significant structural correlation with respect to the size, shape, and location of the rhyolitic zone across density, resistivity, and seismic velocity models; however, there is disagreement with respect to the lateral location of the basaltic zone between our inverse models and the seismic. This depth is where the electromagnetics dominate in the joint inversion, and it is possible the differences in seismic and MT station placements and the inversion methods could be the cause. The next step will be joint inversion of seismic, gravity, and MT data to address this issue. Expandability is a key strength of the Gramian constraint. The determinant in Eq. (8) can be expanded to a 3 × 3 with respect to the three models; however, regularization of a parametric functional incorporating three or more data sets is non-trivial.

A comparison of the convergence behavior of the standalone and joint inversion is shown in Fig. 9. The observed and predicted data for profile AA′ are shown in Fig. 10. The vertical sections of the inverse solutions along profile line BB′ are shown in Fig. 11, and with the Huang et al. (2015) seismic velocity model superimposed in Fig. 12.

The volumes and melt fractions are estimated from inverted resistivity values and Archie's law (Archie, 1942; Yoshino et al., 2010). Based on a mean temperature of 800 °C, an assumption of 8% hydrous fluid and CO_2 (Chu et al., 2010), and a bulk resistivity isosurface of 10 Ohm-m, we estimate a melt fraction of ~19% and total volume of 8400 km^3 for the rhyolitic zone. Similarly, based on a mean

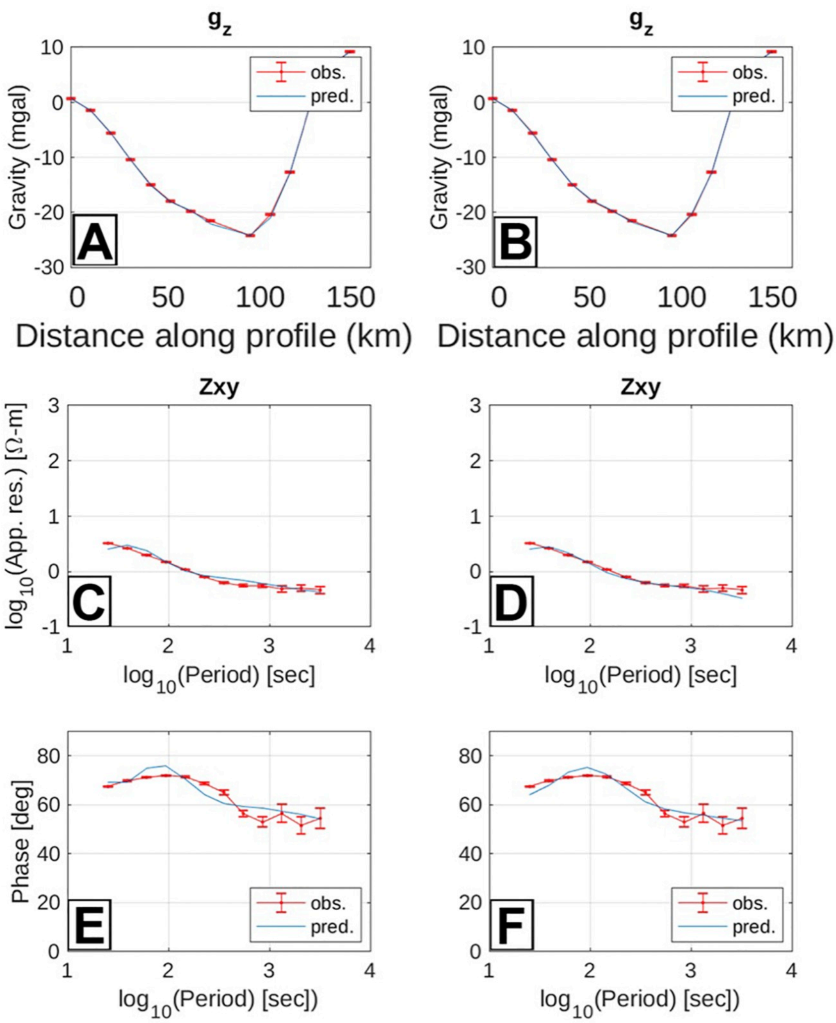

Fig. 10. Comparison of the observed and predicted data for standalone and joint inversions. The observed data are shown by the red lines and the blue lines depict the predicted data. Panels A and B show the comparison between the observed and predicted gravity data along profile AA′ shown in Fig. 4 obtained by standalone and joint inversions, respectively. Panels C and D show the comparison between the observed and predicted apparent resistivity for the XY principal impedance at the MT site shown by the green triangle in Fig. 4 obtained by standalone and joint inversions, respectively. Panels E and F show the comparison between the observed and predicted phase for the XY principal impedance at the same site obtained by standalone and joint inversions, respectively. (For interpretation of the references to color in this figure legend, the reader is referred to the web version of this article.)

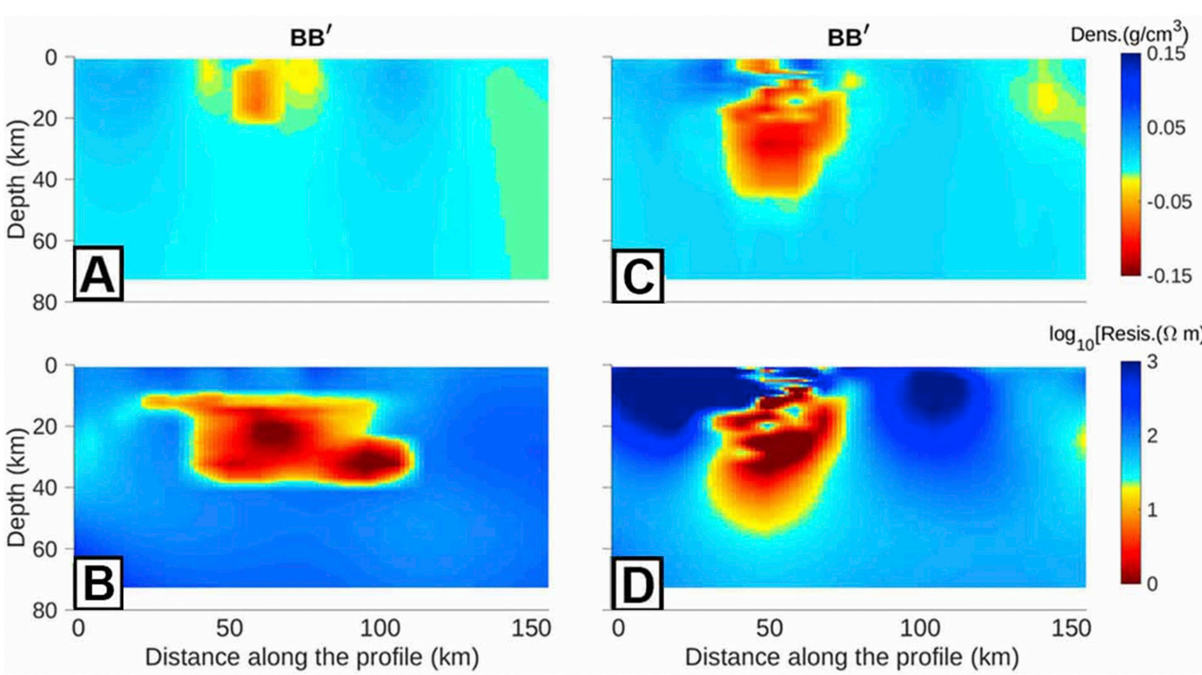

Fig. 11. Comparison of standalone and joint inverse solutions – vertical sections along line BB′. Panels A and B show the standalone inverted anomalous density and total resistivity models, respectively. Panels C and D present the jointly inverted density and resistivity models, respectively.

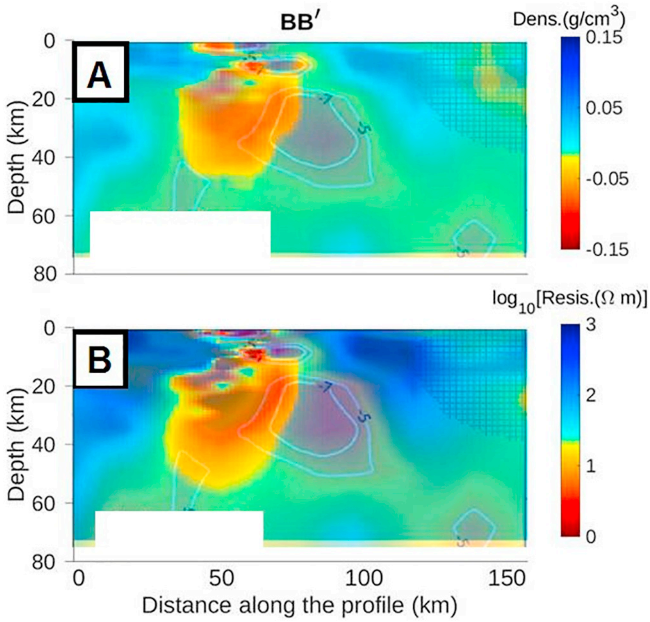

Fig. 12. Vertical sections of the joint inverse solutions along profile line BB′ with seismic velocity model from Huang et al., 2015 superimposed. Panel A shows the jointly inverted density model. Panel B shows the jointly inverted resistivity model.

Table 1
Estimates of melt fractions and total melt volumes of the upper crustal rhyolitic and lower crustal basaltic zones of partial melt.

	Rhyolitic zone	Basaltic zone
Mean temperature	800 °C	1100 °C
H_2O and CO_2	8%	1%
Bulk resistivity	10 Ohm-m	5 Ohm-m
Melt fraction	19%	5%
Total volume	8400 km^3	20,900 km^3
Melt volume	1600 km^3	1000 km^3

temperature of 1100 °C, an assumption of ~1% hydrous fluid (Leeman et al., 2009), and a bulk resistivity isosurface of 5 Ohm-m, we estimate a melt fraction of ~5% and total volume of 20,900 km^3 for the basaltic zone. Multiplying the total volumes by the melt fractions yields 1600 km^3 rhyolitic melts and 1000 km^3 basaltic melts. The estimate of rhyolitic melts is comparable to the last eruption which ejected 1000 km^3 of rhyolitic material (Christiansen, 2001), and the estimate of basaltic melts can explain the large CO_2 flux seen in the caldera. This data is summarized in Table 1.

7. Conclusions

We have developed a method of joint inversion of gravity and MT data based on Gramian constraints and applied it to imaging the deep magma-feeding structure of the Yellowstone supervolcano. Our implementation is based on the integral equation method for computing gravity and MT data, and on the regularized conjugate gradient method for minimization of the joint parametric functional.

The synthetic model study demonstrates that the jointly inverted models tend to more accurately represent the geomorphology of the target versus the separately inverted models, while still maintaining the same level of data misfit. We have applied the developed method to data collected around the Yellowstone volcanic region. The recovered density and resistivity distributions provide a consistent model of both the upper-crustal rhyolitic zone of partial melt and the lower-crustal basaltic zone of partial melt–satisfying expectations from modern mantle plume models. Future research will focus on extending these results by jointly inverting existing seismic, gravity, and MT data acquired around Yellowstone using the developed Gramian approach to data fusion.

Acknowledgements

We acknowledge the support of the Consortium for Electromagnetic Modeling and Inversion (CEMI) at the University of Utah and TechnoImaging. The MT data used in this study were acquired by the Incorporated Research Institutions for Seismology (IRIS) as part of the EarthScope/USArray project (www.earthscope.org;EAR-0323309), supported by the National Science Foundation. The gravity data were acquired primarily by the USGS and made available through PACES at the University of Texas at El Paso (www.research.utep.edu). The PACES database is no longer supported; however, data associated with this article can be found at https://www.dropbox.com/sh/ms4hz3u997uszue/AAAQtQkBfix3E3Uvuw8xFdera?dl=0

References

Archie, G.E., 1942. Electrical resistivity log as an aid determining some reservoir characteristics. In: Transactions of the American Institute of Mining and Metallurgical Engineers. 146. pp. 54–62.
Boyd, F.R., 1961. Welded tuffs and flows in the rhyolite plateau of Yellowstone Park, Wyoming. Geol. Soc. Am. Bull. 72, 387–426.
Christiansen, R.L., 2001. The Quaternary and Pliocene Yellowstone Plateau Volcanic Field of Wyoming, Idaho, and Montana. United States Geological Survey Professional. (Paper 729-G).
Chu, R., Helmberger, D.V., Sun, D., Jackson, J.M., Zhu, L., 2010. Mushy magma beneath Yellowstone. Geophys. Res. Lett. 37, L01306.
Colombo, D., Rovetta, D., 2018. Geophysical joint inversion with multiple coupling operators. Society of Exploration Geophysicists Technical Program Expanded Abstracts 2018, 2292–2296.
Cuma, M., Gribenko, A., Zhdanov, M.S., 2017. Inversion of magnetotelluric data using integral equation approach with variable sensitivity domain: application to EarthScope MT data. Phys. Earth Planet. Inter. 270, 113–127.
DeNosaquo, K.R., Smith, R.B., Lowry, A.R., 2009. Density and lithospheric strength models of the Yellowstone-Snake River Plain volcanic system from gravity and heat flow data. J. Volcanol. Geotherm. Res. 188, 108–127.
DeStefano, M., Andreasi, F.G., Re, S., Virgilio, M., Snyder, F.F., 2011. Multiple-domain, simultaneous joint inversion of geophysical data with application to subsalt imaging. Geophysics 76, R69–R80.
Farrell, J., Smith, R.B., Husen, S., Diehl, T., 2014. Tomography from 26 years of seismicity revealing that the spatial extent of the Yellowstone crustal magma reservoir extends well beyond the Yellowstone caldera. Geophys. Res. Lett. 41, 3068–3073.
Gallardo, L.A., Meju, M.A., 2003. Characterization of heterogeneous near-surface materials by joint 2D inversion of DC resistivity and seismic data. Geophys. Res. Lett. 30, 1658.
Glen, J.M.G., Ponce, D.A., 2002. Large-scale fractures related to inception of the Yellowstone hotspot. Geology 30, 647–650.
Gribenko, A.V., Zhdanov, M.S., 2015. 3D inversion of regional MT data distorted by near-surface inhomogeneities using a complex distortion matrix. In: Society of Exploration Geophysicists Technical Program Expanded Abstracts. 2015. pp. 984–989.
Gribenko, A.V., Zhdanov, M.S., 2017. 3-D inversion of the MT EarthScope data collected over the east central United States. Geophys. Res. Lett. 44, 11800–11807.
Haber, E., Oldenburg, D., 1997. Joint inversion: a structural approach. Inverse Prob. 13, 63–77.
Hadley, D.M., Stewart, G.S., Ebel, J.E., 1976. Yellowstone: seismic evidence for a chemical mantle plume. Science 193, 1237–1239.
Hinze, W.J., Aiken, C., Brozena, J., Coakley, B., Dater, D., Flanagan, G., Forsberg, R., Hildenbrand, T., Keller, G.R., Kellogg, J., Kucks, R., Lee, X., Mainville, A., Morin, R., Pilkington, M., Plouff, D., Ravat, D., Roman, D., Urrutia-Fucugauchi, J., Veronneau, M., Webring, M., Winester, D., 2005. New standards for reducing gravity data: the North American gravity database. Geophysics 70, J25–J32.
Hinze, W.J., VonFrese, R.R.B., Saad, A.H., 2013. Gravity and Magnetic Exploration: Principles, Practices, and Applications. Cambridge University Press.
Huang, H., Lin, F., Schmandt, B., Farrell, J., Smith, R.B., Tsai, V.C., 2015. The Yellowstone magmatic system from the mantle plume to the upper crust. Science 348, 773–776.
Hursan, G., Zhdanov, M.S., 2002. Contraction integral equation method in three-dimensional electromagnetic modeling. Radio Sci. 37, 1–13.
Kelbert, A., Egbert, G.D., deGroot Hedlin, C., 2012. Crust and upper mantle electrical conductivity beneath the Yellowstone hotspot track. Geology 40, 447–450.
Leeman, W.P., Schutt, D.L., Hughes, S.S., 2009. Thermal structure beneath the Snake River Plain: implications for the Yellowstone hotspot. J. Volcanol. Geotherm. Res. 188, 57–67.
Lowenstern, J.B., Hurwitz, S., 2008. Monitoring a supervolcano in repose: heat and volatile flux at the Yellowstone caldera. Elements 4, 35–40.
Meqbel, N.M., Egbert, G.D., Wannamaker, P.E., Kelbert, A., Schultz, A., 2014. Deep

electrical resistivity structure of the northwestern U.S. derived from 3-D inversion of USArray magnetotelluric data. Earth Planet. Sci. Lett. 402, 290–304.

Moorkamp, M., Roberts, A.W., Jegen, M., Heincke, B., Hobbs, R.W., 2013. Verification of velocity-resistivity relationships derived from structural joint inversion with borehole data. Geophys. Res. Lett. 40, 3596–3601.

Morgan, W.J., 1971. Convection plumes in the lower mantle. Nature 230, 42–43.

Smith, R.B., Braile, L.W., 1994. The Yellowstone hotspot. J. Volcanol. Geotherm. Res. 61, 121–129.

Smith, R.B., Jordan, M., Steinberger, B., Puskas, C.M., Farrell, J., Waite, G.P., Husen, S., Chang, W., O'Connell, R., 2009. Geodynamics of the Yellowstone hotspot and mantle plume: seismic and GPS imaging, kinematics, and mantle flow. J. Volcanol. Geotherm. Res. 188, 26–56.

Steinberger, B., Sutherland, R., O'Connell, R.J., 2004. Prediction of Emperor-Hawaii seamount locations from a revised model of global plate motion and mantle flow. Nature 430, 167–173.

Tikhonov, A.N., Arsenin, V.Y., 1977. Solutions of ill-posed problems. V. H. In: Winston.

Yoshino, T., Laumonier, M., McIsaac, E., Katsura, T., 2010. Electrical conductivity of basaltic and carbonatite melt-bearing peridotites at high pressures: implications for melt distribution and melt fraction in the upper mantle. Earth Planet. Sci. Lett. 295, 593–602.

Zhdanov, M.S., 2015. Inverse Theory and Applications in Geophysics. Elsevier.

Zhdanov, M.S., 2018. Foundations of Geophysical Electromagnetic Theory. Elsevier.

Zhdanov, M.S., Keller, G.V., 1992. Electrical Methods in Geophysical Prospecting. Elsevier.

Zhdanov, M.S., Smith, R.B., Gribenko, A.V., Cuma, M., Green, M., 2011. Three-dimensional inversion of large-scale EarthScope magnetotelluric data based on the integral equation method: geoelectrical imaging of the Yellowstone conductive mantle plume. Geophys. Res. Lett. 38.

Zhdanov, M.S., Gribenko, A.V., Wilson, G., 2012. Generalized joint inversion of multimodal geophysical data using Gramian constraints. Geophys. Res. Lett. 39.

Zhdanov, M.S., Zhu, Y., Endo, M., Kinakin, Y., 2016. Novel approach to joint 3D inversion of EM and potential field data using Gramian constraints. First Break 34, 59–64.

Zoback, M.L., Thompson, G.A., 1978. Basin and range rifting in northern Nevada: clues from a mid-Miocene rift and its subsequent offsets. Geology 6, 111–116.